

The data-driven localized wave solutions of the derivative nonlinear Schrödinger equation by using improved PINN approach

Juncai Pu^a, Weiqi Peng^a, Yong Chen^{a,b,*}

^a School of Mathematical Sciences, Shanghai Key Laboratory of Pure Mathematics and Mathematical Practice, East China Normal University, Shanghai, 200241, China

^b College of Mathematics and Systems Science, Shandong University of Science and Technology, Qingdao, 266590, China

ARTICLE INFO

Article history:

Received 28 June 2021

Received in revised form 19 August 2021

Accepted 27 August 2021

Available online 30 August 2021

Keywords:

The data-driven localized wave solutions
The derivative nonlinear Schrödinger equation
Improved physics-informed neural networks

ABSTRACT

The research of the derivative nonlinear Schrödinger equation (DNLS) has attracted more and more extensive attention in theoretical analysis and physical application. The improved physics-informed neural network (IPINN) approach with neuron-wise locally adaptive activation function is presented to derive the data-driven localized wave solutions, which contain rational solution, soliton solution, rogue wave, periodic wave and rogue periodic wave for the DNLS with initial and boundary conditions in complex space. Especially, the flow-process diagram that accounts for the IPINN of DNLS equation has been outline in detail, and the data-driven periodic wave and rogue periodic wave of the DNLS are investigated by employing the IPINN method for the first time. The numerical results indicate the IPINN method can well simulate the localized wave solutions of the DNLS. Furthermore, the relevant dynamical behaviors, error analysis and vivid plots have been exhibited in detail.

© 2021 Elsevier B.V. All rights reserved.

1. Introduction

With the revolution of hardware technology, the great improvement of computer speed and the explosive growth of available data, promoting the application of machine learning and data analysis in practice has made very important progress in pattern recognition, natural language processing, computer vision, cognitive science, genomics and many other fields [1–6]. As is known to all, neural networks (NNs) is an extensive parallel interconnected network composed of adaptive simple units, its organization can simulate the interaction of biological neural system to real world objects [7]. Furthermore, the deep learning of multilayer NNs can solve many practical problems, it has attracted more and more attention in recent years [4–6]. However, in the process of analyzing complicated mathematical, physical, biological and engineering systems, the cost of data acquisition is generally too high, how to utilize machine learning approach to draw conclusions and make decisions under the small data regime is a significant practical problem. In addition, under the environment with only partial information, the vast majority of state-of-the-art machine learning technologies, such as convolution and recurrent NNs [8,9], lack robustness and fail to provide any guarantee of convergence. Recently, a new NNs which also be called physics-informed neural networks (PINNs) has been proposed and proved to be particularly

* Corresponding author at: School of Mathematical Sciences, Shanghai Key Laboratory of Pure Mathematics and Mathematical Practice, East China Normal University, Shanghai, 200241, China.

E-mail address: ychen@sei.ecnu.edu.cn (Y. Chen).

suitable for solving and inverting equations which have been controlled via mathematical physical systems based on the deep learning models of multilayer NNs, and found that the high-dimensional network tasks can be completed with less data sets [10]. That is the PINNs method with the small data regime can not only accurately solve both forward problems, where the approximate solutions of governing equations are obtained, but also precisely deal with the highly ill-posed inverse problems, where parameters involved in the governing equation are inferred from the training data. Subsequently, in order to improve the convergence rate and training effect for PINNs, Jagtap and collaborators presented two different kinds of adaptive activation functions, namely global adaptive activation functions and locally adaptive activation functions, to approximate smooth and discontinuous functions as well as solutions of linear and nonlinear partial differential equations, and introduced a scalable parameters in the activation function, which can be optimized to achieve best performance of the network as it changes dynamically the topology of the loss function involved in the optimization process [11,12]. Moreover, compared with global adaptive activation functions, the numerical results demonstrate the locally adaptive activation functions further improve the training speed and performance of NNs [12]. Furthermore, a slope recovery term based on activation slope has been added to the loss function of locally adaptive activation functions to further improve the performance and speed up the training process of NNs.

In nonlinear optics, many nonlinear models can describe the excitation, propagation and evolution of optical solitons in specific scenes. The soliton transmission in different forms can be described with the use of nonlinear Schrödinger equations, related research indicates that the transmission of solitons can be adjusted with the group velocity dispersion and Kerr nonlinearity coefficients, and the phase shift, amplification, oscillation and attenuation of solitons can also be controlled by other related parameters [13]. The specific coupled nonlinear Schrödinger equation can control the evolution of spatial solitons in photovoltaic photorefractive crystals [14], and by adjusting values of diffraction, width and phase chirp parameters of wave for the $(2 + 1)$ -dimensional nonautonomous-coupled nonlinear Schrödinger equation, the maximum value of the accumulated time can be modulated [15]. Under a constraint among parameters of nonlinear dispersion, nonlinearity and self-steepening perturbation, some new exact analytical solutions of the space-time fractional Fokas–Lenells equation including bright soliton, dark soliton, combined soliton and periodic solutions are found, and the role of fractional order parameters in optical soliton transmission is studied [16]. Furthermore, The derivative nonlinear Schrödinger equation (DNLS) plays a significant role both in the integrable system theory and many physical applications, especially in space plasma physics and nonlinear optics [17,18]. In 1976, Mio and co-workers first derived the DNLS from Alfvén wave propagation in plasma, and found it well described the propagation of small amplitude nonlinear Alfvén wave in low plasma [19]. Furthermore, it was shown that the DNLS can describe the behavior of large-amplitude magnetohydrodynamic waves propagating in an arbitrary direction with respect to the magnetic field in a high- β plasma as well [20]. In nonlinear optics, the DNLS also describes the transmission of sub-picosecond pulses in single mode optical fibers [21], and the DNLS can be derived in the theory of ultrashort femtosecond nonlinear pulse in optical fiber [22]. In electromagnetism, the filamentation of lower-hybrid waves can be simulated by the DNLS which governs the asymptotic state of the filamentation, and it admits moving solitary envelope solutions for the electric field [23]. Therefore, it is very significant to find abundant solutions of the DNLS for explaining various complex physical phenomena and revealing more unknown physical laws.

For decades, some classical solutions and important results of the DNLS have been obtained with the aid of different approaches. In 1978, Kaup and Newell demonstrated the integrability of the DNLS in the sense of inverse scattering method [17]. Furthermore, with the aid of the Hirota bilinear method, the N -soliton formula of the DNLS has been first constructed by Nakamura and Chen [24]. According to the Darboux transform approach, Huang and Chen derived the determinant form of N -soliton formula [25]. Kamchatnov and cooperators not only proposed a method for constructing periodic solutions of several integrable evolution equations and applied it to the DNLS, but also found the formation of solitons on the sharp front of optical pulse in an optical fiber via the DNLS [26,27]. Moreover, Hayashi and Ozawa discussed the Cauchy problem of the DNLS in detail [28]. The compact N -soliton formulae both with asymptotically vanishing and non-vanishing amplitudes were pursued by iterating Bäcklund transformation of the DNLS [29]. Recently, various methods have been utilized to reveal more abundant solutions and more new physical phenomena of the DNLS. By means of certain limit technique, two kinds of generalized Darboux transformations are constructed for the DNLS [30]. Furthermore, in terms of Darboux transformation theory, the mixed interactions of localized waves in the three-component coupled DNLS have been constructed [31], the breather and breather-rogue wave on a periodic background for the DNLS have been investigated [32], the general N -order phase solutions and rogue waves of the DNLS are derived from the trivial seed by using the determinant representation [33], and the generate higher order position solutions and rogue wave solutions for the DNLS are studied [34]. The rogue wave, rational traveling solution, breather solution, periodic solution, dark and bright solitons of the DNLS are given explicitly by substituting different seed solutions into N -fold Darboux transformation [35]. Some important research results for the DNLS are also obtained by utilizing other methods, Zhang and Yan reported a rigorous theory of the inverse scattering transforms for the DNLS with both zero boundary conditions and nonzero boundary conditions at infinity and double zeros of analytical scattering coefficients [36], and general rogue waves are derived for the generalized DNLS equations by a bilinear Kadomtsev–Petviashvili reduction method [37]. The accurate rogue waves on the periodic background of the DNLS has been studied emphatically, the first-order and second-order rogue wave on a periodic background are obtained based on the Darboux transformation, and the second-order rogue wave can display either a fundamental pattern or a triangle pattern on the periodic background by taking a certain perturbation coefficient to eigenfunction [38]. In addition, Chen and Pelinovsky have studied the rogue waves and

algebraic solitons arising on the background of periodic standing waves in the DNLS [39]. Although correlative methods and theories of explicit solutions of DNLS have become increasingly mature, it is still a difficult problem to obtain the solutions of DNLS via numerical method with small data samples.

Recently, recovering the data-drive solutions and revealing the dynamic behaviors of nonlinear partial differential equations with physical constraints have attracted extensive attention and set off a research boom by using the PINN method [10]. Due to the abundant sample space and good properties of integrable systems, it has become a research hotspot to apply the PINN approach to the field of integrable systems, and an effective numerical calculation method and complete theory will be established. More recently, Chen research team constructed a great quantity data-driven solutions for many nonlinear integrable systems by using PINN deep learning method. Li and Chen obtained abundant dynamic behaviors of exact solutions for some second-order and third-order nonlinear evolution partial differential equations via the PINN framework [40,41]. It is worth mentioning that the data-driven rogue periodic wave of nonlinear partial differential equation has been learned by applying multi-layer PINN for the first time [42]. For non-integrable nonlinear system, the data-driven rogue wave solutions and parameter discovery of the defocusing nonlinear Schrödinger equation with the time-dependent potential have also been studied by using PINN method [43]. Moreover, Fang and collaborators firstly extended the PINN to investigate the high-order nonlinear Schrödinger equation and predicted a variety of femtosecond optical soliton excitations in fiber, the unknown physical parameters are studied by using rogue wave solutions as data sets [44]. Especially, the solitons, breathers and rogue wave solutions of the nonlinear Schrödinger equation have been recovered with the help of the PINN model [45]. Furthermore, an improved PINN (IPINN) approach with neuron-wise locally adaptive activation function was presented to derive rational soliton solutions and rogue wave solutions of the DNLS in complex space, and numerical results demonstrated the improved approach has faster convergence and better simulation effect than classical PINN method [46]. In this paper, we will consider localized wave solutions which contain periodic wave solution, rogue wave solution, rogue periodic wave solution and rational solutions of the DNLS by utilizing the IPINN approach with neuron-wise locally adaptive activation function [12,46]. We focus on the following DNLS with initial–boundary value conditions, whose dispersion term is different from that of the DNLS in Ref. [46], the expression is as follows

$$\begin{cases} q_t + iq_{xx} + (|q|^2q)_x = 0, & x \in [L_0, L_1], t \in [T_0, T_1], \\ q(x, T_0) = q_0(x), & x \in [L_0, L_1], \\ q(L_0, t) = q_{lb}(t), & q(L_1, t) = q_{ub}(t), t \in [T_0, T_1], \end{cases} \quad (1.1)$$

where the subscripts denote the partial derivatives of the complex field $q(x, t)$ with respect to the space x and time t , and the L_0 and L_1 represent the lower and upper boundaries of x respectively. Similarly, T_0 and T_1 represent the initial and final times of t respectively. Moreover, the $q_{lb}(t)$ and $q_{ub}(t)$ are the lower and upper boundaries of the $q(x, t)$ corresponding to $x = L_0$ and $x = L_1$ respectively.

This paper is organized as follows. In Section 2, we introduce briefly discussions of the IPINN method with locally adaptive activation function, where also discuss about training data, loss function, optimization method and the operating environment. Moreover, the algorithm flow schematic of the DNLS based on IPINN model is exhibited in detail. In Section 3, the data-driven rational soliton, rational phase solution and vivid plots of DNLS have been exhibited via IPINN model. Section 4 provides the periodic wave, rogue wave and rogue periodic wave of the DNLS by utilizing the improved PINN approach, and related plots and dynamic analysis are given out in detail. Conclusion is given out in last section.

2. The improved PINN method

In general, we consider the general $(1 + 1)$ -dimensional nonlinear time-dependent equations in complex space, in which each contains a dissipative term as well as other partial derivatives, such as nonlinear terms or dispersive terms, as shown below

$$q_t + \mathcal{N}(q, q_x, q_{xx}, q_{xxx}, \dots) = 0, \quad (2.1)$$

where q are complex-valued solutions of x and t to be determined later, and \mathcal{N} is a nonlinear functional which contains the solution $q(x, t)$, its derivatives of arbitrary order respecting to x and any combination between them. Due to the complexity of the structure of the complex-valued solutions $q(x, t)$ in Eq. (2.1), we decompose $q(x, t)$ into the real part $u(x, t)$ and the imaginary part $v(x, t)$ by employing two real-valued functions $u(x, t)$ and $v(x, t)$, that is $q(x, t) = u(x, t) + iv(x, t)$. Then substituting it into Eq. (2.1), we have

$$u_t + \mathcal{N}_u(u, u_x, u_{xx}, u_{xxx}, \dots) = 0, \quad (2.2)$$

$$v_t + \mathcal{N}_v(v, v_x, v_{xx}, v_{xxx}, \dots) = 0. \quad (2.3)$$

Similarly, the \mathcal{N}_u and \mathcal{N}_v are nonlinear functionals which consist of the corresponding solutions, their derivatives of arbitrary order respecting to x and any combination between them, respectively. Then the physics-informed neural networks $f_u(x, t)$ and $f_v(x, t)$ can be defined as

$$f_u := u_t + \mathcal{N}_u(u, u_x, u_{xx}, u_{xxx}, \dots), \quad (2.4)$$

$$f_v := v_t + \mathcal{N}_v(v, v_x, v_{xx}, v_{xxx}, \dots). \tag{2.5}$$

The original PINN method could not accurately reconstruct solutions of complex forms in some complicated nonlinear equations. Therefore, due to some accuracy and performance requirements, we draw into an IPINN where a neuron-wise locally adaptive activation function technique is introduced into the classical PINN method in this paper. It changes the slope of the activation function adaptively, resulting in non-vanishing gradients and faster training of the network. Specifically, we first define such neuron-wise locally adaptive activation function as

$$\sigma(na_i^d(\mathcal{L}_d(\mathbf{x}^{d-1}))_i), d = 1, 2, \dots, D-1, i = 1, 2, \dots, N_d,$$

where $n > 1$ is a scaling factor and $\{a_i^d\}$ are additional $\sum_{d=1}^{D-1} N_d$ parameters to be optimized. Note that, there is a critical scaling factor n_c , and the optimization algorithm will become sensitive when $n \geq n_c$ in each problem set. The neuron activation function acts as a vector activation function in each hidden layer, and each neuron has its own slope of activation function.

The new NN with neuron-wise locally adaptive activation function can be represented as

$$q(\mathbf{x}; \bar{\Theta}) = (\mathcal{L}_D \circ \sigma \circ na_i^{D-1}(\mathcal{L}_{D-1})_i \circ \dots \circ \sigma \circ na_i^1(\mathcal{L}_1)_i)(\mathbf{x}), \tag{2.6}$$

where the set of trainable parameters $\bar{\Theta} \in \bar{\mathcal{P}}$ consists of $\{\mathbf{W}^d, \mathbf{b}^d\}_{d=1}^D$ and $\{a_i^d\}_{i=1}^{D-1}, \forall i = 1, 2, \dots, N_d, \bar{\mathcal{P}}$ is the parameter space. In this method, the initialization of scalable parameters are carried out in the case of $na_i^d = 1, \forall n \geq 1$.

The resulting optimization algorithm will attempt to find the optimized parameters including the weights, biases and additional coefficients in the activation to minimize the new loss function defined as

$$Loss = Loss_q + Loss_f + Loss_a, \tag{2.7}$$

where $Loss_q, Loss_f$ are defined as following

$$Loss_q = \frac{1}{N_q} \left[\sum_{i=1}^{N_q} |u(x_u^i, t_u^i) - u^i|^2 + \sum_{i=1}^{N_q} |v(x_v^i, t_v^i) - v^i|^2 \right], \tag{2.8}$$

and

$$Loss_f = \frac{1}{N_f} \left[\sum_{j=1}^{N_f} |f_u(x_f^j, t_f^j)|^2 + \sum_{j=1}^{N_f} |f_v(x_f^j, t_f^j)|^2 \right], \tag{2.9}$$

where $\{x_u^i, t_u^i, u^i\}_{i=1}^{N_q}$ and $\{x_v^i, t_v^i, v^i\}_{i=1}^{N_q}$ denote the initial and boundary value data on Eqs. (2.2) and (2.3). Furthermore, $\{x_f^j, t_f^j\}_{j=1}^{N_f}$ represent the collocation points on networks $f_u(x, t)$ and $f_v(x, t)$. The last slope recovery term $Loss_a$ in the loss function (2.5) is defined as

$$Loss_a = \frac{1}{\frac{N_a}{D-1} \sum_{d=1}^{D-1} \exp\left(\frac{\sum_{i=1}^{N_d} a_i^d}{N_d}\right)}, \tag{2.10}$$

where N_a has been imposed to control the range of the value size of $Loss_a$, and we all take $N_a = 10$ for dominating the loss function and ensuring that the loss value is not too large in this paper. Here, term $Loss_q$ forces the NN to increase the activation slope value quickly, which ensures the non-vanishing of the gradient of the loss function and improves the network's training speed. Consequently, $Loss_q$ corresponds to the loss on the initial and boundary data, the $Loss_f$ penalizes the DNLS not being satisfied on the collocation points, and the $Loss_a$ changes the topology of $Loss$ function and improves the convergence speed and network optimization ability. Moreover, in order to better measure the training error, we introduce \mathbb{L}_2 norm error, which is defined as follows

$$\mathbb{L}_2 \text{ Error} = \frac{\sqrt{\sum_{i=1}^N |q^{\text{exact}}(\mathbf{x}_i) - q^{\text{predict}}(\mathbf{x}_i; \bar{\Theta})|^2}}{\sqrt{\sum_{i=1}^N |q^{\text{exact}}(\mathbf{x}_i)|^2}},$$

where $q^{\text{predict}}(\mathbf{x}_i; \bar{\Theta})$ and $q^{\text{exact}}(\mathbf{x}_i)$ represent the model training prediction solution and exact analytical solution at point $\mathbf{x}_i = (x_i, t_i)$, respectively.

In order to understand IPINN approach more clearly, the IPINN algorithm flow model of the DNLS is shown in following. Fig. 1 gives a sketch of IPINN algorithm for the DNLS where one can see the NN along with the supplementary physics-informed part. The loss function is evaluated using the contribution from the NN part as well as the residual from the governing equation given by the physics-informed part. Then, one seeks the optimal values of weights \mathbf{W} , biases \mathbf{b} and

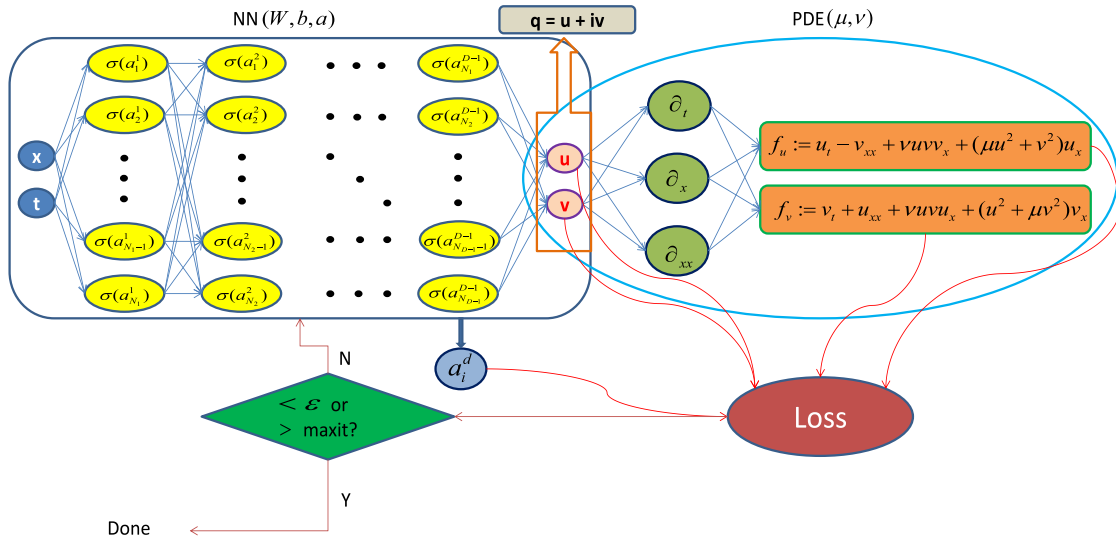


Fig. 1. (Color online) Schematic of IPINN for the DNLS. The left NN is the uninformed network while the right one induced by the governing equation is the informed network. The two NNs share hyper-parameters and they both contribute to the loss function.

scalable parameter a_i^d in order to minimize the loss function below certain tolerance ε until a prescribed maximum number of iterations.

In this method, all loss functions are simply optimized by employing the L-BFGS algorithm, which is a full-batch gradient descent optimization algorithm based on a quasi-Newton method [47]. Especially, the scalable parameters in the adaptive activation function are initialized generally as $n = 5$, $a_i^d = 0.2$, unless otherwise specified. In addition, we select relatively simple multi-layer perceptrons (i.e., feedforward NNs) with the Xavier initialization and the hyperbolic tangent (tanh) as activation function. All the codes in this article is based on Python 3.7 and Tensorflow 1.15, and all numerical experiments reported here are run on a DELL Precision 7920 Tower computer with 2.10 GHz 8-core Xeon Silver 4110 processor and 64 GB memory.

3. The data-driven rational solution and soliton solution of the DNLS

In this section, we numerically reveal two different types of solutions and their corresponding dynamic analysis for the DNLS by using the IPINN which contains nine hidden layers with each layer having 40 neurons. The accurate rational solution and soliton solution have been obtained by using the Darboux transformation [33].

3.1. The data-driven rational solution

It is known that Eq. (1.1) admits the explicit rational solution [33]

$$q_{rs}(x, t) = \frac{4e^{2i(2t-x)}(4i(4t-x)-1)^3}{(16(4t-x)^2+1)^2}. \quad (3.1)$$

In what follows, we will consider the initial condition $q_{rs}(x, T_0)$ and Dirichlet boundary condition $q_{rs}(L_0, t)$ and $q_{rs}(L_1, t)$ of Eq. (1.1) arising from the rational solution Eq. (3.1). Here we take $[L_0, L_1]$ and $[T_0, T_1]$ in Eq. (1.1) as $[-5.0, 5.0]$ and $[-0.08, 0.08]$, respectively. Then, we focus on the corresponding the Cauchy problem with initial condition $q_0(x)$, as shown below

$$q_{rs}(x, -0.08) = \frac{4e^{2i(-0.16-x)}(4i(-0.32-x)-1)^3}{(16(-0.32-x)^2+1)^2}, \quad x \in [-5.0, 5.0], \quad (3.2)$$

and the Dirichlet boundary conditions

$$q_{lb}(t) = q_{rs}(-5.0, t), \quad q_{ub}(t) = q_{rs}(5.0, t), \quad t \in [-0.08, 0.08]. \quad (3.3)$$

We employ the traditional finite difference scheme on even grids in MATLAB to simulate Eq. (3.1) which contains the initial data (3.2) and boundary data (3.3) to acquire the training data. Specifically, divide spatial region $[-5.0, 5.0]$ into 513 points and temporal region $[-0.08, 0.08]$ into 401 points, rational solution (3.1) is discretized into 401 snapshots accordingly. We generate a smaller training dataset containing initial-boundary data by randomly extracting $N_q = 400$ from original dataset and $N_f = 20000$ collocation points which are generated by the Latin hypercube sampling method

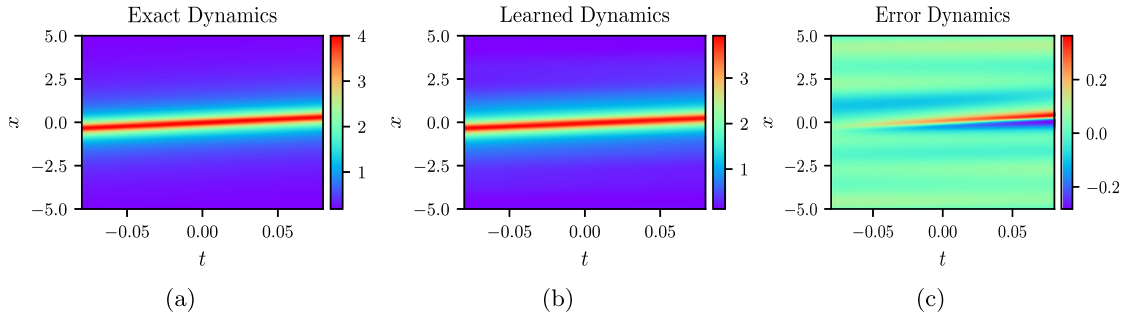


Fig. 2. (Color online) The rational solution $q(x, t)$ based on the IPINN: (a) The density plot of exact rational solution; (b) The density plot of learned rational solution; (c) The error density plot of the difference between exact and learned rational solution.

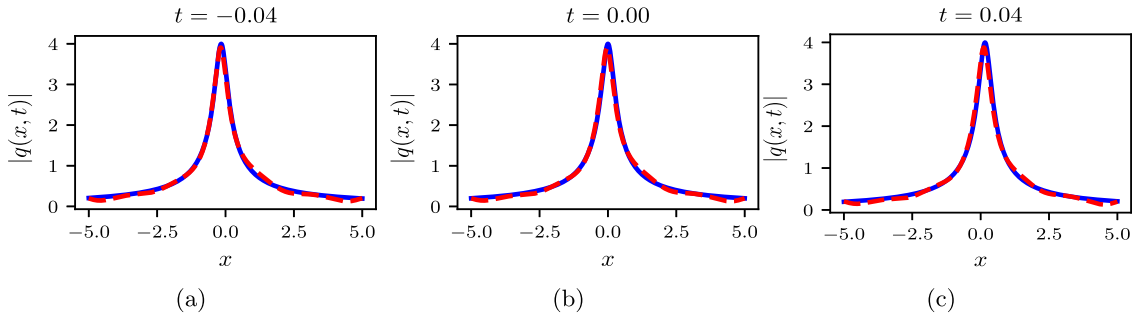


Fig. 3. (Color online) The sectional drawings of rational solution $q(x, t)$ based on the IPINN at (a): $t = -0.04$, (b): $t = 0$ and (c): $t = 0.04$.

(LHS) [48]. After giving a dataset of initial and boundary points, the latent rational solution $q(x, t)$ has been successfully learned by tuning all learnable parameters of the IPINN and regulating the loss function (2.7). The model of IPINN achieves a relative \mathbb{L}_2 error of $6.042053e-02$ in about 1159.0106 s, and the number of iterations is 7448.

In Figs. 2–4, the density plots, the sectional drawing at different times and the iteration number curve plots for the rational solution $q(x, t)$ under IPINN structure are plotted respectively. Specifically, the density plots of exact dynamics, learned dynamics and error dynamics have exhibited in detail, and the corresponding peak scale is shown on the right side of the density plots in Fig. 2. Specially, from Fig. 2(c), one can obviously find that the error range is about -0.2 to 0.2 . In Fig. 3, we provide the sectional drawings of rational solution $q(x, t)$ based on the IPINN at (a): $t = -0.04$, (b): $t = 0$ and (c): $t = 0.04$, and infer that the rational solution propagates right along the x -axis. The three-dimensional plot and its corresponding contour map of rational solution for the DNLS (1.1) has been given out in the left panel (a) of Fig. 4. From the right panel (a) of Fig. 4, we can observe that the $Loss$ curve (red solid line) and the $Loss_q$ curve (blue solid line) converge smoothly, and the $Loss_q$ curve decreases faster. However, the $Loss_f$ curve (yellow solid line) fluctuates greatly and has poor stability. On the contrary, $Loss_a$ curve (green solid line) decreases slowly around 0.01 and has a strong stability.

3.2. The data-driven soliton solution

The explicit soliton solution has been obtained in Ref. [33], one can be written as below

$$q_{ss}(x, t) = \frac{2i \left[-\frac{1}{2} \operatorname{icosh}(-6t + 2x) + \sinh(-6t + 2x) \right]^3 e^{2i \left(-\frac{7}{8}t - \frac{3}{4}x \right)}}{\left\{ -\frac{5}{4} [\cosh(-6t + 2x)]^2 + 1 \right\}^2}. \tag{3.4}$$

Compared with the nonlinear Schrödinger equation (NLS) [45], the form of the soliton solution for the DNLS is more complex, and it is more difficult to recover the soliton solution by NNs. Similarly, considering the initial condition $q_{ss}(x, T_0)$ and Dirichlet boundary conditions $q_{ss}(L_0, t)$ and $q_{ss}(L_1, t)$ of Eq. (1.1) arising from the soliton solution Eq. (3.4), we take $[L_0, L_1]$ and $[T_0, T_1]$ in Eq. (1.1) as $[-3.0, 3.0]$ and $[-0.1, 0.1]$, respectively. After that, the corresponding Cauchy problem with initial condition $q_0(x)$ can be written as below

$$q_{ss}(x, -0.1) = \frac{2i \left[-\frac{1}{2} \operatorname{icosh}(0.6 + 2x) + \sinh(0.6 + 2x) \right]^3 e^{2i \left(0.0875 - \frac{3}{4}x \right)}}{\left\{ -\frac{5}{4} [\cosh(0.6 + 2x)]^2 + 1 \right\}^2}, \quad x \in [-3.0, 3.0], \tag{3.5}$$

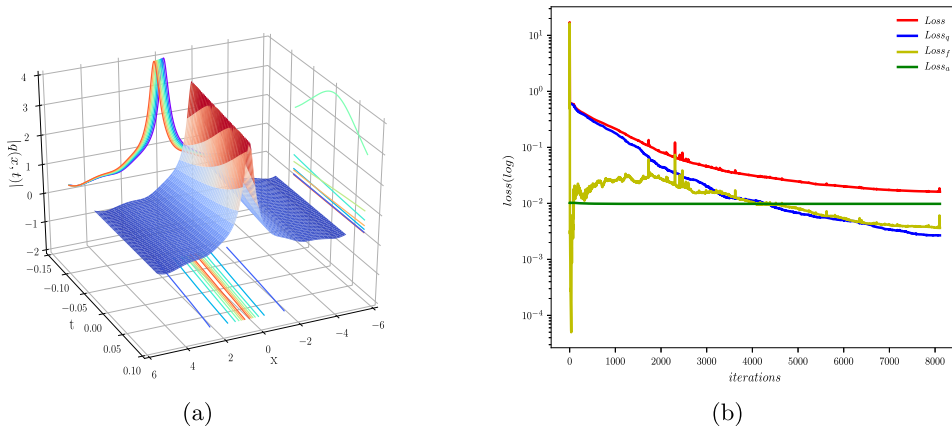


Fig. 4. (Color online) The rational solution $q(x, t)$ based on the IPINN: (a) The three-dimensional plot; (b) The loss curve figure.

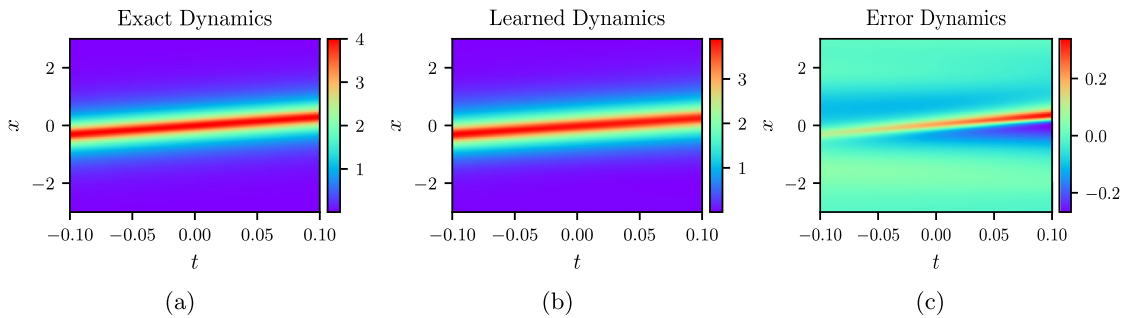


Fig. 5. (Color online) The soliton solution $q(x, t)$ based on the IPINN: (a) The density plot of exact soliton solution; (b) The density plot of learned soliton solution; (c) The error density plot of the difference between exact and learned soliton solution.

and the Dirichlet boundary conditions in Eq. (1.1) become

$$q_{lb}(t) = q_{ss}(-3.0, t), \quad q_{ub}(t) = q_{ss}(3.0, t), \quad t \in [-0.1, 0.1]. \tag{3.6}$$

In MATLAB, we discretize the Eq. (3.4) by applying the traditional finite difference scheme on even grids, and obtain the training data which contains initial data (3.5) and boundary data (3.6) by dividing the spatial region $[-3.0, 3.0]$ into 513 points and the temporal region $[-0.1, 0.1]$ into 401 points. We generate a smaller training dataset containing initial-boundary data by randomly extracting $N_q = 400$ from original dataset and $N_f = 20000$ collocation points which are generated by employing LHS. After giving a dataset of initial and boundary points, the latent soliton solution $q(x, t)$ has been successfully learned by tuning all learnable parameters of the IPINN and regulating the loss function (2.7). The model of IPINN achieves a relative \mathbb{L}_2 error of $5.745440e-02$ in about 1417.7192 s, and the number of iterations is 8472.

In Figs. 5–7, the density plots, the sectional drawing at different times and the iteration number curve plots for the soliton solution $q(x, t)$ under IPINN structure are plotted respectively. Specifically, the density plots of exact dynamics, learned dynamics and error dynamics have exhibited in detail, and the corresponding peak scale is shown on the right side of the density plots in Fig. 5. Similar to Fig. 2(c), it is obvious that the error range is also about -0.2 to 0.2 from Fig. 5(c). In Fig. 6, the sectional drawings with different time point for soliton solution $q(x, t)$ have been given out respectively. Similarly with Section 3.1, when the increase of time t , the soliton solution propagates from left to right along the x -axis. The left panel (a) of Fig. 7 exhibits the three-dimensional plot and its corresponding contour map of soliton solution for the DNLS (1.1). From the right panel (b) of Fig. 7, one can observe that the $Loss$ curve (red solid line) and the $Loss_q$ curve (blue solid line) converge smoothly, and the $Loss_q$ curve decreases faster. On the other hand, the $Loss_f$ curve (yellow solid line) fluctuates greatly and has poor stability. Similarly, $Loss_a$ curve (green solid line) decreases slowly around 0.01 and has a strong stability.

Comparing the rational solution with the soliton solution, we can find that the two solutions have different forms, in which the initial and boundary conditions of the rational solution is simpler, but the shapes of the two solutions are similar. Through a large number of numerical training experiments, we find that it is more difficult to simulate the rational solution and the soliton solution for the DNLS than the NLS equation, and the range of time t should not be too large, otherwise the training error will become large.

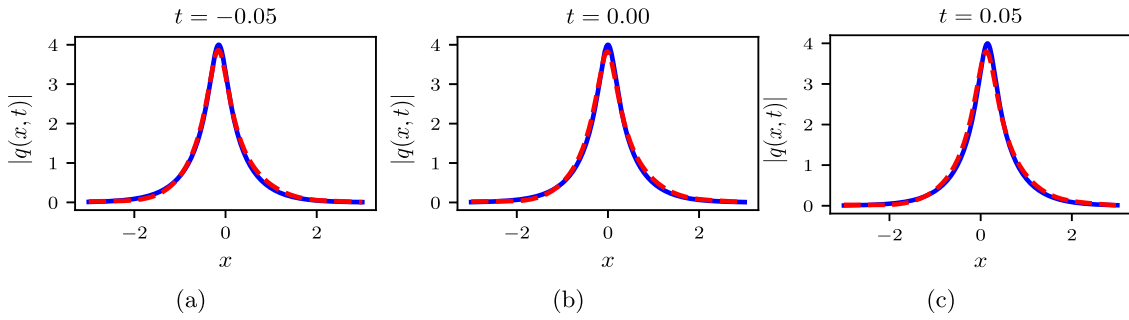


Fig. 6. (Color online) The sectional drawings of soliton solution $q(x, t)$ based on the IPINN at (a): $t = -0.05$, (b): $t = 0$ and (c): $t = 0.05$.

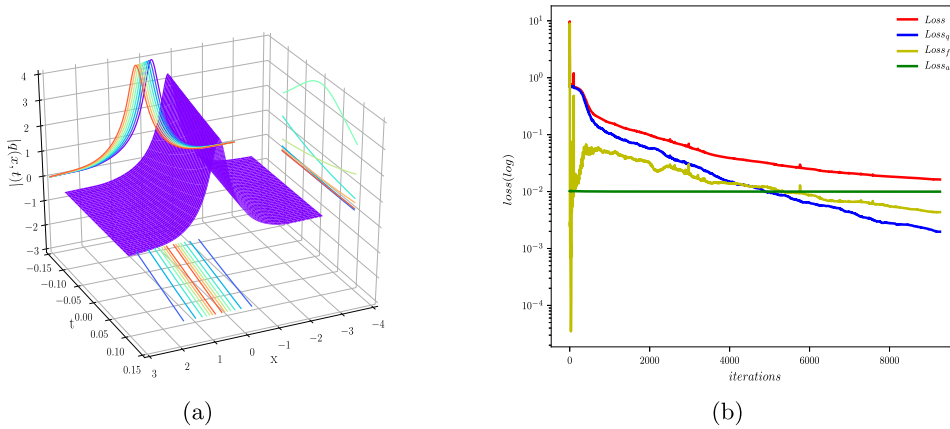


Fig. 7. (Color online) The soliton solution $q(x, t)$ based on the IPINN: (a) The three-dimensional plot; (b) The loss curve figure.

4. The data-driven periodic wave, rogue wave and rogue periodic wave of the DNLS

It is well known that periodic waves and rogue waves are very significant waves in nonlinear integrable systems, and the periodic wave and rogue wave of the DNLS have been also widely studied [29,30,32–35,37–39,46]. However, to the best of our knowledge, the mixtures of periodic solutions and rogue-wave solutions for the DNLS were not considered up to now by utilizing deep learning method based on NNs. Thus, it is interesting and necessary to find the data-driven rogue periodic wave solution describing the behavior of rogue waves on a periodic background. In Ref. [46], Pu et al. have investigated the rational solutions and two order rogue wave solution for another form of the DNLS by classical PINN and IPINN, and pointed out the IPINN has more advantages about the overall effect, especially in simulation of the complex rogue wave solutions. Furthermore, as far as we know, the periodic wave and one order rogue wave of the DNLS have also not been investigated yet by employing PINNs technique. Therefore, in this section, we will devote to investigate the data-driven periodic wave, rogue wave and rogue periodic wave of the DNLS with the aid of IPINN, which consists of nine hidden layers and each layer has 40 neurons.

4.1. The data-driven periodic wave solution

From Ref. [38], the explicit periodic wave solution of the DNLS can be obtained as

$$q_{pw}(x, t) = \frac{\left[(\sqrt{5} + 2)e^{\frac{\sqrt{5}}{2}ix} + \left(-\frac{1}{2} - \frac{\sqrt{5}}{2}\right)e^{\frac{\sqrt{5}}{2}i(t-x)} + \left(-\frac{3}{2} - \frac{\sqrt{5}}{2}\right)e^{\frac{\sqrt{5}}{4}it} \right] e^{-ix}}{\left[e^{\frac{\sqrt{5}}{4}ix} + \left(\frac{3}{2} + \frac{\sqrt{5}}{2}\right)e^{\frac{\sqrt{5}}{4}i(t-x)} \right]^2}. \tag{4.1}$$

Eq. (4.1) is a periodic wave solution which is periodic in space x , and it is obvious that the period is 3 when $x \in [-6, 12]$, the amplitude of each wave crest and trough of wave is 2 and 0, respectively. Since the waveforms of periodic waves on both sides of time $t = 0$ are the same, the range of time t does not need to be symmetric about $t = 0$. Therefore, one can take $[L_0, L_1]$ and $[T_0, T_1]$ in Eq. (1.1) as $[-6.0, 12.0]$ and $[0.0, 2.0]$ in this subsection, respectively. The corresponding Cauchy problem with the initial condition $q_0(x)$ of Eq. (1.1) arising from the periodic wave solution Eq. (4.1) can be written

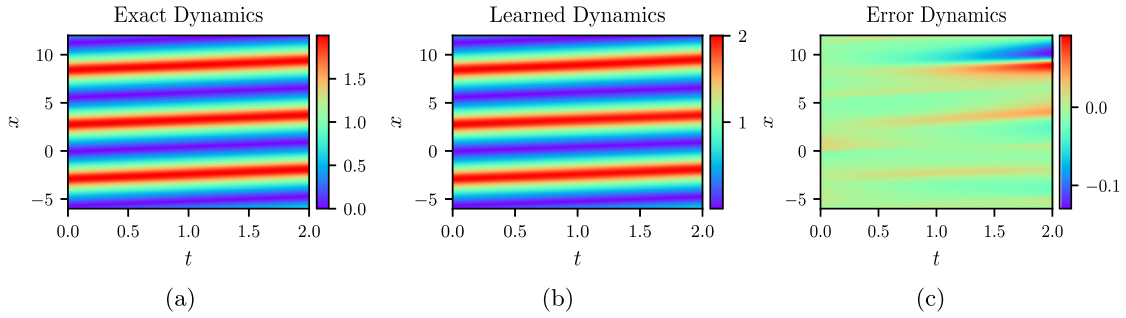


Fig. 8. (Color online) The periodic wave solution $q(x, t)$ based on the IPINN: (a) The density plot of exact periodic wave solution; (b) The density plot of learned periodic wave solution; (c) The error density plot of the difference between exact and learned periodic wave solution.

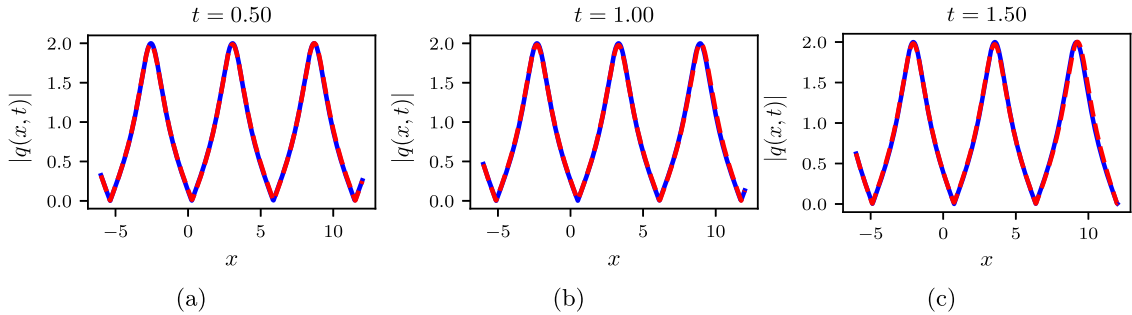


Fig. 9. (Color online) The sectional drawings of periodic wave solution $q(x, t)$ based on the IPINN at (a): $t = 0.50$, (b): $t = 1.00$ and (c): $t = 1.50$.

as below

$$q_{pw}(x, 0.0) = \frac{[(\sqrt{5} + 2)e^{\frac{\sqrt{5}}{2}ix} + (-\frac{1}{2} - \frac{\sqrt{5}}{2})e^{-\frac{\sqrt{5}}{2}ix} - \frac{3}{2} - \frac{\sqrt{5}}{2}]e^{-ix}}{[e^{\frac{\sqrt{5}}{4}ix} + (\frac{3}{2} + \frac{\sqrt{5}}{2})e^{-\frac{\sqrt{5}}{4}ix}]^2}, \quad x \in [-6.0, 12.0], \quad (4.2)$$

and the Dirichlet boundary conditions $q(L_0, t)$ and $q(L_1, t)$ in Eq. (1.1) become as following

$$q_{lb}(t) = q_{pw}(-6.0, t), \quad q_{ub}(t) = q_{pw}(12.0, t), \quad t \in [0.0, 2.0]. \quad (4.3)$$

Similarly, discretizing Eq. (4.1) via the aid of the traditional finite difference scheme on even grids, and obtain the original training data which contain initial data (4.2) and boundary data (4.3) by dividing the spatial region $[-6.0, 12.0]$ into 513 points and the temporal region $[0.0, 2.0]$ into 401 points. Then, one can generate a smaller training dataset that containing initial-boundary data by randomly extracting $N_q = 100$ from original dataset and $N_f = 10000$ collocation points which are produced by the LHS. After that, the latent periodic wave solution $q(x, t)$ has been successfully learned by tuning all learnable parameters of the IPINN and regulating the loss function (2.7). The model of IPINN achieves a relative \mathbb{L}_2 error of $2.035710e-02$ in about 2827.0457 s, and the number of iterations is 20157.

In Figs. 8–10, the density plots, the sectional drawing at different times and the Loss curve plots for the periodic wave solution $q(x, t)$ under IPINN structure are plotted respectively. Specifically, the density plots of exact dynamics, learned dynamics and error dynamics have exhibited in detail, and the corresponding peak scale is shown on the right side of the density plots in Fig. 8. From the striped density map, it is obvious that the periodic wave has three periods and the amplitude is the same. Specially, according to Fig. 8(c), one can obviously find that the error range is about -0.1 to 0.1 , this error range is lower than that of the two data-driven solutions in Section 3. In Fig. 9, we provide the sectional drawings of rational solution $q(x, t)$ based on the IPINN at (a): $t = 0.50$, (b): $t = 1.00$ and (c): $t = 1.50$, and infer that the periodic wave solution propagates right along the x -axis as time t increases. The three-dimensional plot and its corresponding contour map of periodic wave solution for the DNLS (1.1) has been given out in the left panel (a) of Fig. 10. From the right panel (b) of Fig. 10, we can observe that the Loss curve (red solid line) and $Loss_q$ curve (blue solid line) converge smoothly, in which the $Loss_q$ curve decreases faster. However, the $Loss_f$ curve (yellow solid line) fluctuates violently in the first 100 iterations and converges smoothly in the later iterations, the convergence rate of $Loss_f$ is between the Loss curve and the $Loss_q$ curve. Here, $Loss_a$ curve (green solid line) decreases slowly around 0.01 and has a strong stability.

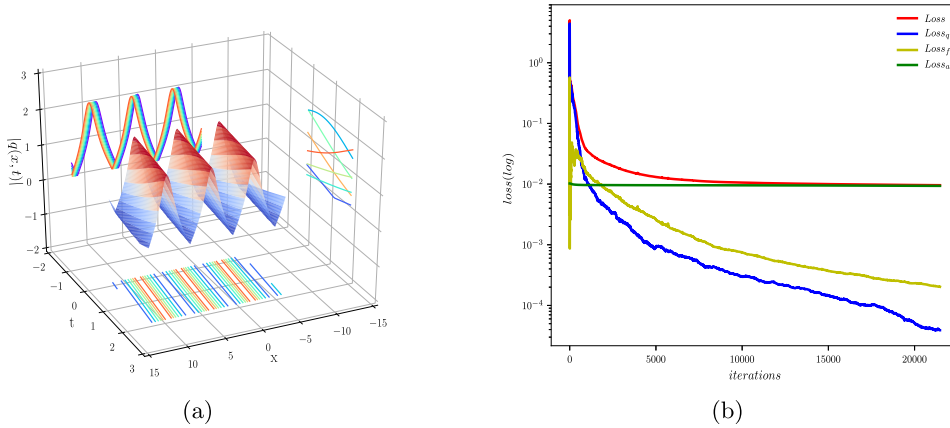


Fig. 10. (Color online) The periodic wave solution $q(x, t)$ based on the IPINN: (a) The three-dimensional plot; (b) The loss curve figure.

4.2. The data-driven rogue wave solution

From Ref. [34], the rogue wave solution of the DNLS can be derived as

$$q_{rw}(x, t) = \frac{[-2t^2 - 2x^2 - 1 - i(-2t + 2x)][2t^2 + 2x^2 - 3 + i(6t + 2x)]e^{ix}}{[-2t^2 - 2x^2 - 1 + i(-2t + 2x)]^2}. \quad (4.4)$$

Similarly, considering the initial condition $q_{rw}(x, T_0)$ and Dirichlet boundary condition $q_{rw}(L_0, t)$ and $q_{rw}(L_1, t)$ of Eq. (1.1) arising from the rogue wave solution Eq. (4.4), the $[L_0, L_1]$ and $[T_0, T_1]$ in Eq. (1.1) are taken as $[-10.0, 10.0]$ and $[-1.0, 1.0]$, respectively. After that, the corresponding Cauchy problem with initial condition $q_0(x)$ can be written as below

$$q_{rw}(x, -1.0) = \frac{[-2 - 2x^2 - 1 - i(2 + 2x)][2 + 2x^2 - 3 + i(-6 + 2x)]e^{ix}}{[-2 - 2x^2 - 1 + i(2 + 2x)]^2}, \quad x \in [-10.0, 10.0], \quad (4.5)$$

and the Dirichlet boundary condition evolve into

$$q_{lb}(t) = q_{rw}(-10.0, t), \quad q_{ub}(t) = q_{rw}(10.0, t), \quad t \in [-1.0, 1.0]. \quad (4.6)$$

Similar to Section 4.1, we discretize the Eq. (4.4) by applying the traditional finite difference scheme on even grids with the help of Matlab, and obtain the training data which contain initial data (4.5) and boundary data (4.6) by dividing the spatial region $[-10.0, 10.0]$ into 513 points and the temporal region $[-1.0, 1.0]$ into 401 points. A smaller training dataset containing initial–boundary data will be generated by randomly extracting $N_q = 400$ from original dataset and $N_f = 20000$ collocation points via LHS. After giving a dataset of initial and boundary points, the latent rogue wave solution $q(x, t)$ has been successfully learned by tuning all learnable parameters of the IPINN and regulating the loss function (2.7). The model of IPINN achieves a relative \mathbb{L}_2 error of $7.459070e-02$ in about 2833.9749 s, and the number of iterations is 18138.

In Figs. 11–13, the density plots, the sectional drawing at different times and the iteration number curve plots for the rogue wave solution $q(x, t)$ under IPINN structure are plotted respectively. Specifically, the density plots with the corresponding peak scale for exact dynamics, learned dynamics and error dynamics have exhibited in Fig. 11. Specially, by analyzing Fig. 11(c), one can obviously find that the error range is about -0.4 to 0.4 , the error range is obviously larger than that in Section 3. In Fig. 12, the sectional drawings for rogue wave solution $q(x, t)$ based on the IPINN at (a): $t = -0.50$, (b): $t = 0$ and (c): $t = 0.50$ have been provide, and inferring that the amplitude of the rogue wave solution reaches the maximum at time $t = 0$, and the waveform of the profiles at time $t = -0.50$ and $t = 0.50$ are symmetrical. The three-dimensional plot with corresponding contour map of rogue wave solution for the DNLS (1.1) has been given out in the left panel (a) of Fig. 13. From the right panel (b) of Fig. 13, we can observe that the Loss curve (red solid line) converge smoothly, and the $Loss_q$ curve (blue solid line) decreases faster. However, when the number of iterations is less than 2500, the $Loss_f$ curve (yellow solid line) fluctuates greatly and has poor stability. Once the number of iterations is greater than 2500, the descent speed of $Loss_f$ curve is almost the same as that of $Loss_q$ curve. The same as before, $Loss_a$ curve (green solid line) decreases slowly around 0.01 and has a strong stability.

4.3. The data-driven rogue periodic wave solution

Compared with the traditional rogue wave which is on plane wave background, the rogue periodic wave is the rogue wave solution on the periodic wave background. From Ref. [34], the rogue periodic wave solution of the DNLS can be

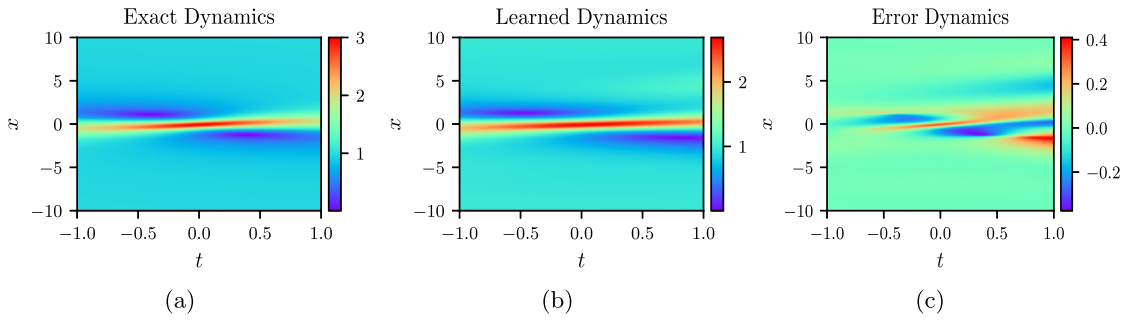


Fig. 11. (Color online) The rogue wave solution $q(x, t)$ based on the IPINN: (a) The density plot of exact rogue wave solution; (b) The density plot of learned rogue wave solution; (c) The error density plot of the difference between exact and learned rogue wave solution.

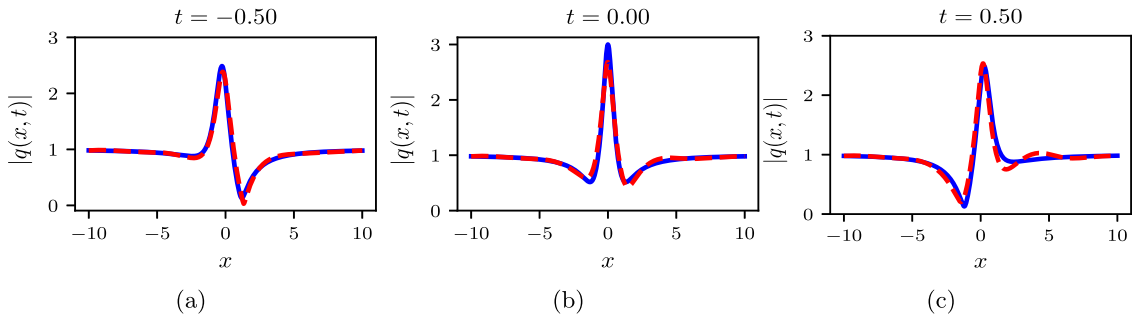


Fig. 12. (Color online) The sectional drawings of rogue wave solution $q(x, t)$ based on the IPINN at (a): $t = -0.5$, (b): $t = 0$ and (c): $t = 0.5$.

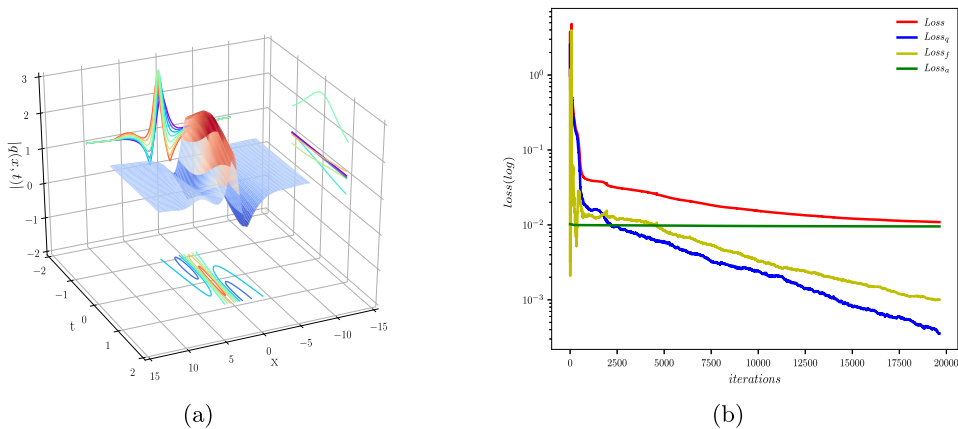


Fig. 13. (Color online) The rogue wave solution $q(x, t)$ based on the IPINN: (a) The three-dimensional plot; (b) The loss curve figure.

obtained as follows

$$q_{\text{rpw}}(x, t) = \frac{\Omega_{11}^2}{\Omega_{21}^2} e^{ix} + 2i \frac{\Omega_{11}\Omega_{12}}{\Omega_{21}^2}, \tag{4.7}$$

where

$$\begin{aligned} \Omega_{11} = & \frac{1}{15625} \left\{ \left[(2498it - 2498ix - 2502t^2 - 2502x^2 - 1251)\sqrt{1562501} + 3119998it - \right. \right. \\ & \left. \left. 3129998ix - 3125002t^2 - 3125002x^2 - 1567501 \right] e^{-\frac{i(t-1250x)\sqrt{1562501}}{3125000} - \frac{ix}{2}} \right\} - \frac{4}{625} \\ & \left[\left(it + ix - t^2 - x^2 + \frac{1}{2} \right) \sqrt{1562501} + 2it + 2500ix + 1251 \right] e^{\frac{i(t-1250x)\sqrt{1562501}}{3125000} - \frac{ix}{2}}, \end{aligned}$$

$$\Omega_{12} = \frac{1}{781250} \left\{ [(-125000it^2 + 62500i - 125000ix^2 + 125000t + 125000x)\sqrt{1562501} - 156250100i(t^2 + x^2) + 78249950i + 156500100t + 156249900x] e^{\frac{-i(t-1250x)\sqrt{1562501}}{3125000} + \frac{ix}{2}} \right\} + \frac{1}{390625} \left\{ 1249 \left[\left(it^2 + ix^2 + \frac{i}{2} + \frac{1251t}{1249} - \frac{1251x}{1249} \right) \sqrt{1562501} - \frac{1562501i}{1249}(t^2 + x^2) + \frac{4687499i}{2498} + \frac{4690001t}{1249} + \frac{1559999x}{1249} \right] e^{\frac{i(t-1250x)\sqrt{1562501}}{3125000} + \frac{ix}{2}} \right\},$$

and

$$\Omega_{21} = \frac{1}{15625} \left\{ [(-2498it - 2502t^2 - 2502x^2 + 2498ix - 1251)\sqrt{1562501} - 3119998it + 3129998ix - 3125002(t^2 + x^2) - 1567501] e^{\frac{i(t-1250x)\sqrt{1562501}}{3125000} + \frac{ix}{2}} \right\} + \frac{4}{625} \left[\left(it + ix + t^2 + x^2 - \frac{1}{2} \right) \sqrt{1562501} + 2it + 2500ix - 1251 \right] e^{\frac{-i(t-1250x)\sqrt{1562501}}{3125000} + \frac{ix}{2}}.$$

Similarly, considering the initial condition $q_{rpw}(x, T_0)$ and Dirichlet boundary conditions $q_{rpw}(L_0, t)$ and $q_{rpw}(L_1, t)$ of Eq. (1.1) arising from the rogue periodic wave solution Eq. (4.7), we set $[L_0, L_1]$ and $[T_0, T_1]$ in Eq. (1.1) as $[-20.0, 20.0]$ and $[-0.5, 0.5]$, respectively. After that, the corresponding Cauchy problem with initial condition $q_0(x)$ can be written as below

$$q_{rpw}(x, -0.5) = \frac{\Omega_{11}'^2}{\Omega_{21}'^2} e^{ix} + 2i \frac{\Omega_{11}' \Omega_{12}'^2}{\Omega_{21}'^2}, \quad x \in [-20.0, 20.0], \tag{4.8}$$

where

$$\Omega_{11}' = \frac{1}{15625} \left\{ [(-1249i - 2498ix - 625.5 - 2502x^2 - 1251)\sqrt{1562501} - 1559999i - 3129998ix - 781250.5 - 3125002x^2 - 1567501] e^{\frac{-i(-0.5-1250x)\sqrt{1562501}}{3125000} - \frac{ix}{2}} \right\} - \frac{4}{625} \left[\left(-0.5i + ix - 0.25 - x^2 + \frac{1}{2} \right) \sqrt{1562501} - i + 2500ix + 1251 \right] e^{\frac{i(-0.5-1250x)\sqrt{1562501}}{3125000} - \frac{ix}{2}},$$

$$\Omega_{12}' = \frac{1}{781250} \left\{ [(-31250i + 62500i - 125000ix^2 - 62500 + 125000x)\sqrt{1562501} - 156250100i(0.25 + x^2) + 78249950i - 78250050 + 156249900x] e^{\frac{-i(-0.5-1250x)\sqrt{1562501}}{3125000} + \frac{ix}{2}} \right\} + \frac{1}{390625} \left\{ 1249 \left[\left(0.25i + ix^2 + \frac{i}{2} + \frac{-625.5}{1249} - \frac{1251x}{1249} \right) \sqrt{1562501} - \frac{1562501i}{1249}(0.25 + x^2) + \frac{4687499i}{2498} + \frac{-2345000.5}{1249} + \frac{1559999x}{1249} \right] e^{\frac{i(-0.5-1250x)\sqrt{1562501}}{3125000} + \frac{ix}{2}} \right\},$$

and

$$\Omega_{21}' = \frac{1}{15625} \left\{ [(1249i - 625.5 - 2502x^2 + 2498ix - 1251)\sqrt{1562501} + 1559999i + 3129998ix - 3125002(0.25 + x^2) - 1567501] e^{\frac{i(-0.5-1250x)\sqrt{1562501}}{3125000} + \frac{ix}{2}} \right\} + \frac{4}{625} \left[\left(-0.5i + ix + 0.25 + x^2 - \frac{1}{2} \right) \sqrt{1562501} - i + 2500ix - 1251 \right] e^{\frac{-i(-0.5-1250x)\sqrt{1562501}}{3125000} + \frac{ix}{2}}.$$

The Dirichlet boundary condition is

$$q_{lb}(t) = q_{rpw}(-20.0, t), \quad q_{ub}(t) = q_{rpw}(20.0, t), \quad t \in [-0.5, 0.5]. \tag{4.9}$$

Here, applying the same data discretization method in Section 4.1, and producing the training data which consists of initial data (4.8) and boundary data (4.9) by dividing the spatial region $[-20.0, 20.0]$ into 513 points and the temporal region $[-0.5, 0.5]$ into 401 points. We generate a smaller training dataset that containing initial-boundary data by randomly extracting $N_q = 600$ from original dataset and $N_f = 20000$ collocation points which are generated by the Latin hypercube sampling method. After giving a dataset of initial and boundary points, the latent rogue periodic wave solution $q(x, t)$ has been successfully learned by tuning all learnable parameters of the IPINN and regulating the loss function (2.7). The model of IPINN achieves a relative \mathbb{L}_2 error of $8.766380e-02$ in about 3862.2879 s, and the number of iterations is 22414.

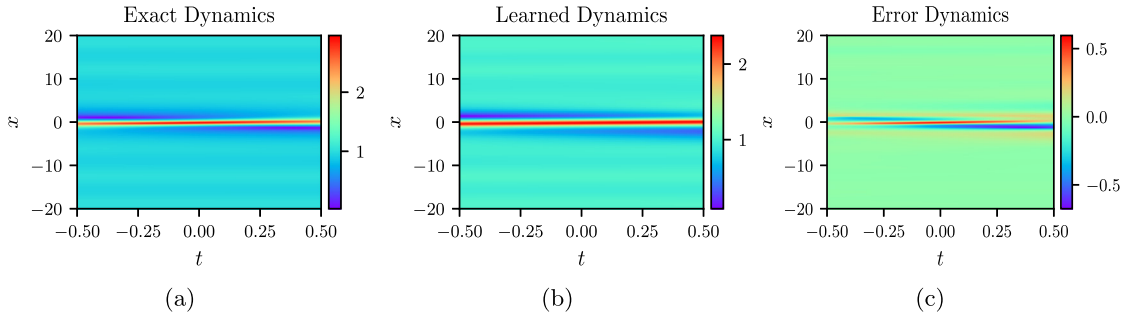


Fig. 14. (Color online) The rogue periodic wave solution $q(x, t)$ based on the IPINN: (a) The density plot of exact rogue periodic wave solution; (b) The density plot of learned rogue periodic wave solution; (c) The error density plot of the difference between exact and learned rogue periodic wave solution.

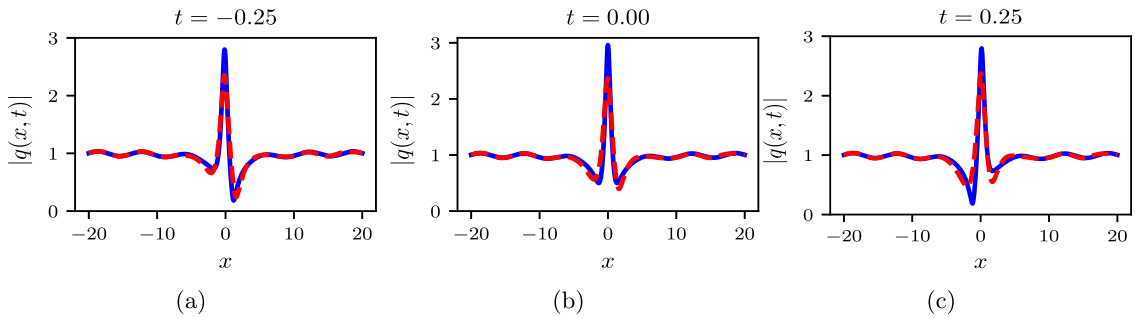


Fig. 15. (Color online) The sectional drawings of rogue periodic wave solution $q(x, t)$ based on the IPINN at (a): $t = -0.5$, (b): $t = 0$ and (c): $t = 0.5$.

In Figs. 14–16, the density plots, the sectional drawing at different times and the iteration number curve plots for the rogue periodic wave solution $q(x, t)$ under IPINN structure are plotted respectively. Specifically, the density plots of exact dynamics, learned dynamics and error dynamics have exhibited in detail, and the corresponding peak scale is shown on the right side of the density plots in Fig. 14. Specially, from Fig. 14(c), one can obviously find that the error range is about -0.2 to 0.2 . In Fig. 15, we provide a comparison between the exact rogue periodic wave solution and the predicted solution based on the IPINN at different instants (a): $t = -0.25$, (b): $t = 0$ and (c): $t = 0.25$, and infer that the amplitude of the rogue wave solution reaches the maximum at time $t = 0$, and the waveform of the profiles at time $t = -0.25$ and $t = 0.25$ are symmetrical. The three-dimensional plot and its corresponding contour map of rogue periodic wave solution for the DNLS (1.1) has been given out in the left panel (a) of Fig. 16. From the right panel (b) of Fig. 16, it is obvious that the $Loss$ curve (red solid line), $Loss_q$ curve (blue solid line) and $Loss_f$ curve (yellow solid line) arise oscillation before about 10 000 iterations, especially $Loss_f$ curve oscillates most violently. After 10 000 iterations, the three kinds of curves converge smoothly, and $Loss_q$ converges the fastest. Due to characteristics of $Loss_a$, the $Loss_a$ curve (green solid line) decreases steadily and slowly around 0.01.

5. Conclusion

Increasing the performance of deep learning algorithms is significant in order to design fast and accurate machine learning techniques. An IPINN framework for extracting localized wave solutions dynamics of $(1 + 1)$ -dimensional nonlinear time-dependent systems has been introduced from the spatiotemporal data. Specifically, we outline the flow-process diagram of DNLS equation based on the IPINN in detail. In this paper, we are committed to research the data-driven localized wave solutions which contain rational solution, soliton solution, periodic wave solution, rogue wave solution and rogue periodic wave solution for the DNLS by employing IPINN approach under the condition of small sample data set. The results show that the IPINN model could recover the different dynamical behaviors of localized wave solutions for DNLS fairly well.

Compared with the nonlinear Schrödinger equation and Chen–Lee–Liu equation, the DNLS has more nonlinear terms, so it is more difficult to recover data-driven solutions of the DNLS than the nonlinear Schrödinger equation and Chen–Lee–Liu equation [42,45,46]. As we can see from the Sections 3 and 4, it can be found that the \mathbb{L}_2 norm error cannot reach the order of magnitude $e-03$ by using IPINN method to recover the data-driven localized wave solutions with corresponding initial and boundary conditions. Moreover, we find that the data-driven localized wave solutions cannot be recovered well when the temporal region t is too wide. Therefore, we can find that more nonlinear terms have a greater impact on

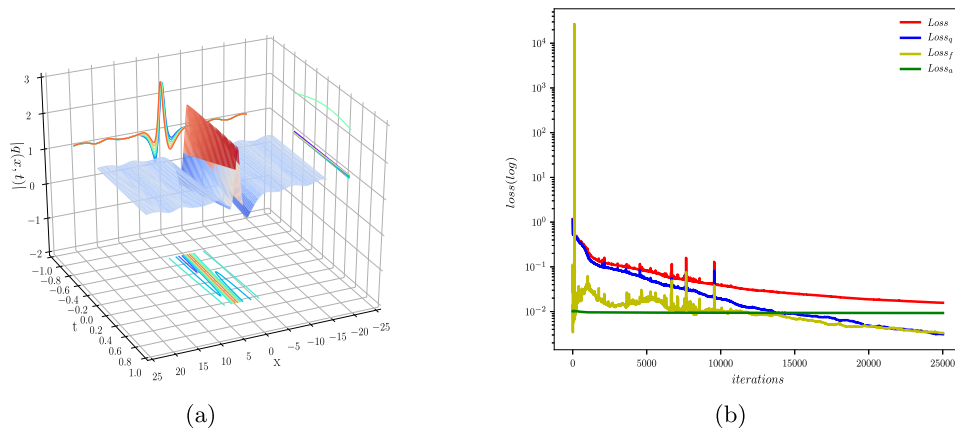


Fig. 16. (Color online) The rogue periodic wave solution $q(x, t)$ based on the IPINN: (a) The three-dimensional plot; (b) The loss curve figure.

the performance of the neural network. Although higher order dispersion terms also have an impact on the performance of the neural network, the impact is not as violent as the nonlinear terms.

Compared with the classical PINN method, the influence of $Loss_q$ and $Loss_f$ on $Loss$ of IPINN approach is negligible due to the introduction of $Loss_a$. Generally speaking, from Sections 3 and 4, it is obvious that the curve of $Loss_f$ fluctuates violently when the number of iterations is small, while the $Loss_a$ in all models decreases steadily around 0.01, which is determined by its slope mathematical structure. In the training process by employing IPINN method, the values of $Loss_q$ and $Loss_f$ are usually far less than the value of $Loss_a$, so their mathematical sum is mainly dominated according to $Loss_a$ and the Eq. (2.7), and $Loss_a$ is very stable, which ensures the overall topological stability of loss function. Although the values of $Loss_q$ and $Loss_f$ are larger than that of $Loss_a$ when simulating some complex solutions, for example, one can see that although the loss curve has obvious fluctuation in the early stage of training, the overall decline trend is stable and the decline is more and more stable after the iteration times are larger in Section 4.3. Apparently, $Loss_a$ plays an important role in the IPINN model, we can control the slope stability interval of $Loss$ by controlling the size of N_a . If N_a is too small, the overall $Loss$ target value is too large. Conversely, if N_a is too large, $Loss_a$ cannot lead the loss function well, which will affect the stability of $Loss$ curve.

Compared with the traditional numerical methods, the IPINN has no limitation of grid size and large data set, and gives full play to the advantages of computer science and neural network. Moreover, the IPINN approach is trained with just few data, fast convergence speed and has a better physical interpretability by applying the physical constraints and locally adaptive activation function. The IPINN method showcases a series of results of various problems in the interdisciplinary field of applied mathematics and computational science, and opens a new path for using deep learning to simulate unknown solutions and correspondingly discover the parametric equations in scientific computing. It also provides a theoretical and practical basis for solving some high-dimensional scientific and big data space-time problems that cannot be solved before. However, for the nonlinear integrable systems which contain high order nonlinear term is an unavoidable research hotspot. How to use the theory of integrable systems to improve IPINN model is a problem that needs further research in the future.

CRedit authorship contribution statement

Juncai Pu: Conceptualization, Methodology, Design, Formal analysis, Software, Validation, Writing – original draft, Writing – review & editing. **Weiqli Peng:** Conceptualization, Formal analysis. **Yong Chen:** Supervision, Writing – review & editing.

Declaration of competing interest

The authors declare that they have no known competing financial interests or personal relationships that could have appeared to influence the work reported in this paper.

Acknowledgments

The authors gratefully acknowledge the support of the National Natural Science Foundation of China (No. 12175069), the Global Change Research Program of China (No. 2015CB953904), and Science and Technology Commission of Shanghai Municipality (No. 18dz2271000).

References

- [1] Y. LeCun, Y. Bengio, G. Hinton, Deep learning, *Nature* 521 (2015) 436–444.
- [2] C.M. Bishop, *Pattern Recognition and Machine Learning*, Springer Press, New York, 2006.
- [3] R. Collobert, J. Weston, G. Bottou, M. Karlen, K. Kavukcuoglu, P. Kuksa, Natural language processing (almost) from scratch, *J. Mach. Learn. Res.* 12 (2011) 2493–2537.
- [4] A. Krizhevsky, I. Sutskever, G. Hinton, Imagenet classification with deep convolutional neural networks, *Commun. AcM* 60 (2017) 84–90.
- [5] B.M. Lake, R. Salakhutdinov, J.B. Tenenbaum, Human-level concept learning through probabilistic program induction, *Science* 350 (2015) 1332–1338.
- [6] B. Alipanahi, A. DeLong, M.T. Weirauch, B.J. Frey, Predicting the sequence specificities of DNA- and RNA-binding proteins by deep learning, *Nat. Biotechnol.* 33 (2015) 831–838.
- [7] T. Kohonen, An introduction to neural computing, *Neural Netw.* 1 (1988) 3–16.
- [8] Y. LeCun, L.D. Jackel, B. Boser, J.S. Denker, H.P. Graf, I. Guyon, D. Henderson, R.E. Howard, W. Hubbard, Handwritten digit recognition: applications of neural network chips and automatic learning, *IEEE Commun. Mag.* 27 (1989) 41–46.
- [9] D.E. Rumelhart, G.E. Hinton, R.J. Williams, Learning representations by back-propagating errors, *Nature* 323 (1986) 533–536.
- [10] M. Raissi, P. Perdikaris, G.E. Karniadakis, Physics-informed neural networks: A deep learning framework for solving forward and inverse problems involving nonlinear partial differential equations, *J. Comput. Phys.* 378 (2019) 686–707.
- [11] A.D. Jagtap, K. Kawaguchi, G.E. Karniadakis, Adaptive activation functions accelerate convergence in deep and physics-informed neural networks, *J. Comput. Phys.* 404 (2020) 109136.
- [12] A.D. Jagtap, K. Kawaguchi, G.E. Karniadakis, Locally adaptive activation functions with slope recovery for deep and physics-informed neural networks, *Proc. R. Soc. Lond. Ser. A Math. Phys. Eng. Sci.* 476 (2020) 20200334.
- [13] W.T. Yu, Q. Zhou, M. Mirzazadeh, W.J. Liu, A. Biswas, Phase shift, amplification, oscillation and attenuation of solitons in nonlinear optics, *J. Adv. Res.* 15 (2019) 69–76.
- [14] C.Q. Dai, Y.Y. Wang, Coupled spatial periodic waves and solitons in the photovoltaic photorefractive crystals, *Nonlinear Dynam.* 102 (2020) 1733–1741.
- [15] C.Q. Dai, Y.Y. Wang, J.F. Zhang, Managements of scalar and vector rogue waves in a partially nonlocal nonlinear medium with linear and harmonic potentials, *Nonlinear Dynam.* 102 (2020) 379–391.
- [16] B.H. Wang, Y.Y. Wang, C.Q. Dai, Y.X. Chen, Dynamical characteristic of analytical fractional solitons for the space–time fractional fokas-lenells equation, *Alexand. Eng. J.* 59 (2020) 4699–4707.
- [17] D.J. Kaup, A.C. Newell, An exact solution for a derivative nonlinear Schrödinger equation, *J. Math. Phys.* 19 (1978) 798–801.
- [18] E. Mjølhus, On the modulational instability of hydromagnetic waves parallel to the magnetic field, *J. Plasma Phys.* 16 (1976) 321–334.
- [19] K. Mio, T. Ogino, K. Minami, S. Takeda, Modified nonlinear Schrödinger equation for Alfvén waves propagating along the magnetic field in cold plasmas, *J. Phys. Soc. Japan* 41 (1976) 265–271.
- [20] M. Ruderman, Dnls equation for large-amplitude solitons propagating in an arbitrary direction in a high- β Hall plasma, *J. Plasma Phys.* 67 (2002) 271–276.
- [21] N. Tzoar, M. Jain, Self-phase modulation in long-geometry optical waveguides, *Phys. Rev. A* 23 (1981) 1266–1270.
- [22] X.J. Chen, W.K. Lam, Inverse scattering transform for the derivative nonlinear Schrödinger equation with nonvanishing boundary conditions, *Phys. Rev. E* 69 (2004) 066604.
- [23] K.H. Spatckek, P.K. Shukla, M.Y. Yu, Filamentation of lower-hybrid cones, *Nucl. Fusion* 18 (1977) 290–293.
- [24] A. Nakamura, H.H. Chen, Multi-soliton solutions of a derivative nonlinear Schrödinger equation, *J. Phys. Soc. Japan* 49 (1980) 813–816.
- [25] N.N. Huang, Z.Y. Chen, Alfvén solitons, *J. Phys. A: Math. Gen.* 23 (1990) 439–453.
- [26] A.M. Kamchatnov, On improving the effectiveness of periodic solutions of the NLS and DNLS equations, *J. Phys. A: Math. Gen.* 23 (1990) 2945–2960.
- [27] A.M. Kamchatnov, S.A. Darmanyan, F. Lederer, Formation of solitons on the sharp front of the pulse in an optical fiber, *Phys. Lett. A* 245 (1998) 259–264.
- [28] N. Hayashi, T. Ozawa, On the derivative nonlinear Schrödinger equation, *Physica D* 55 (1992) 14–36.
- [29] H. Steudel, The hierarchy of multi-soliton solutions of the derivative nonlinear Schrödinger equation, *J. Phys. A: Math. Gen.* 36 (2003) 1931–1946.
- [30] B.L. Guo, L.M. Ling, Q.P. Liu, High-order solutions and generalized darboux transformations of derivative nonlinear Schrödinger equations, *Stud. Appl. Math.* 130 (2012) 317–344.
- [31] T. Xu, Y. Chen, Mixed interactions of localized waves in the three-component coupled derivative nonlinear Schrödinger equations, *Nonlinear Dynam.* 92 (2018) 2133–2142.
- [32] B. Xue, J. Shen, X.G. Geng, Breathers and breather-rogue waves on a periodic background for the derivative nonlinear Schrödinger equation, *Phys. Scr.* 95 (2020) 055216.
- [33] S.W. Xu, J.S. He, D. Mihalache, Rogue waves generation through multi-He solutions degeneration for the derivative nonlinear Schrödinger equation, *Nonlinear Dynam.* 97 (2019) 2443–2452.
- [34] Y.S. Zhang, L.J. Guo, S.W. Xu, Z.W. Wu, J.S. He, The hierarchy of higher order solutions of the derivative nonlinear Schrödinger equation, *Commun. Nonlinear Sci. Numer. Simul.* 19 (2014) 1706–1722.
- [35] S.W. Xu, J.S. He, L.H. Wang, The darboux transformation of the derivative nonlinear Schrödinger equation, *J. Phys. A* 44 (2011) 305203.
- [36] G.Q. Zhang, Z.Y. Yan, The derivative nonlinear Schrödinger equation with zero/nonzero boundary conditions: inverse scattering transforms and N-double-pole solutions, *J. Nonlinear Sci.* 30 (2020) 3089–3127.
- [37] B. Yang, J.C. Chen, J.K. Yang, Rogue waves in the generalized derivative nonlinear Schrödinger equations, *J. Nonlinear Sci.* 30 (2020) 3027–3056.
- [38] W. Liu, Y.S. Zhang, J.S. He, Rogue wave on a periodic background for kaup-newell equation, *Rom. Rep. Phys.* 70 (2018) 106.
- [39] J.B. Chen, D.E. Pelinovsky, Rogue waves on the background of periodic standing waves in the derivative nonlinear Schrödinger equation, *Phys. Rev. E* 103 (2021) 062206.
- [40] J. Li, Y. Chen, Solving second-order nonlinear evolution partial differential equations using deep learning, *Commun. Theor. Phys.* 72 (2020) 105005.
- [41] J. Li, Y. Chen, A deep learning method for solving third-order nonlinear evolution equations, *Commun. Theor. Phys.* 72 (2020) 115003.
- [42] W.Q. Peng, J.C. Pu, Y. Chen, PINN deep learning for the Chen-Lee-Liu equation: rogue wave on the periodic background, 2021, arXiv:2105.13027.
- [43] L. Wang, Z.Y. Yan, Data-driven rogue waves and parameter discovery in the defocusing nonlinear Schrödinger equation with a potential using the PINN deep learning, *Phys. Lett. A* 404 (2021) 127408.
- [44] Y. Fang, G.Z. Wu, Y.Y. Wang, C.Q. Dai, Data-driven femtosecond optical soliton excitations and parameters discovery of the high-order NLSE using the PINN, *Nonlinear Dynam.* 105 (2021) 603–616.
- [45] J.C. Pu, J. Li, Y. Chen, Soliton, breather and rogue wave solutions for solving the nonlinear Schrödinger equation using a deep learning method with physical constraints, *Chin. Phys. B* 30 (2021) 060202.
- [46] J.C. Pu, J. Li, Y. Chen, Solving localized wave solutions of the derivative nonlinear Schrödinger equation using an improved PINN method, *Nonlinear Dynam.* 105 (2021) 1723–1739.
- [47] D.C. Liu, J. Nocedal, On the limited memory BFGS method for large scale optimization, *Math. Program.* 45 (1989) 503–528.
- [48] M. Stein, Large sample properties of simulations using latin hypercube sampling, *Technometrics* 29 (1987) 143–151.